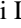





Raman spectroscopy of bimagnon and trimagnon excitations and rotonlike points in a distorted triangular lattice antiferromagnet

Junli Li ^{1,*} Shangjian Jin ^{1,*} Trinanjan Datta ^{2,3,†} and Dao-Xin Yao ^{1,4,‡}

¹State Key Laboratory of Optoelectronic Materials and Technologies, Guangdong Provincial Key Laboratory of Magnetoelectric Physics and Devices, Center for Neutron Science and Technology, School of Physics, Sun Yat-Sen University, Guangzhou 510275, China

²Department of Chemistry and Physics, Augusta University, 1120 15th Street, Augusta, Georgia 30912, USA

³Kavli Institute for Theoretical Physics, University of California, Santa Barbara, California 93106, USA

⁴International Quantum Academy, Shenzhen 518048, China



(Received 13 February 2023; revised 13 April 2023; accepted 18 April 2023; published 2 May 2023)

We investigate the experimental signatures of Raman spectroscopy of bimagnon and trimagnon excitations in the distorted triangular lattice antiferromagnets α - LCr_2O_4 (L =Sr, Ca). Motivated by Raman scattering experiments, we utilize spin wave theory to analyze the nearly 120° spin-3/2 spiral-ordered antiferromagnetic ground state to compute the single-magnon density of states, single-magnon dispersion, and bimagnon and trimagnon Raman spectra (polarized and unpolarized). We perform calculations of the Heisenberg antiferromagnetic Hamiltonian that incorporates magnetic interactions (exchange, anisotropy, and interlayer coupling) and lattice distortion within a four-sublattice unit cell. We investigate the Hamiltonian for both model parameter sets and experimentally proposed magnetic interactions for α - LCr_2O_4 (L =Sr, Ca). It is found that Raman scattering is capable of capturing the effect of the rotonlike M and M' points on the bimagnon Raman spectrum. Our calculation confirms the connection between single-magnon rotonlike excitation energy and the bimagnon Raman excitation spectrum observed experimentally. The roton energy minimum in momentum space is half of the energy of a bimagnon excitation signal. The experimental magnetic Raman scattering result displays two peaks which have Raman shifts of 15 and 40 meV. Theoretical modeling and analysis of the experimental spectrum of α - $SrCr_2O_4$ within our distorted Heisenberg Hamiltonian lattice suggest that the low-energy peak at 15 meV is associated with the bimagnon excitation, whereas the high-energy peak around 40 meV is primarily a trimagnon excitation. Based on our fitting procedure we propose a set of magnetic interaction parameters for α - $SrCr_2O_4$. These parameters reproduce not only the experimental Raman spectrum but also the inelastic neutron scattering response (including capturing high-energy magnon branches). We also compute the unpolarized bimagnon and trimagnon Raman spectra for α - $CaCr_2O_4$. In contrast to its Sr cousin the Ca-based material has an enhanced bimagnon response, with the high-energy peak still dominated by the trimagnon excitation. Furthermore, the polarization sensitivity of the Raman spectrum can be utilized to distinguish the bimagnon and trimagnon excitation channels.

DOI: [10.1103/PhysRevB.107.184402](https://doi.org/10.1103/PhysRevB.107.184402)

I. INTRODUCTION

Experimental [1–4] and theoretical [5–19] studies on triangular lattice antiferromagnets (TLAFs) suggest the stabilization of a long-range-ordered ground state that can be noncollinear and noncoplanar. The noncollinear ordering pattern is due to competing exchange interactions which in a perfect undistorted triangular lattice geometry manifest as a 120° magnetic structure [17,18]. However, distortions of the underlying lattice network due to a heterogeneous magnetic unit cell modify the strength of the exchange interactions. This in turn introduces anisotropic exchange interaction along various crystallographic directions of the lattice. The modified interactions result in a shift of the ordering wave vector, a

behavior supported by theoretical investigation [2] and experimental observations [2,20,21]. TLAFs have been investigated for their spin order and ground states using spin wave theory [8,14,15]. They have also been well studied theoretically and experimentally because of their single-magnon excitation behavior using inelastic neutron scattering (INS) experiments [22,23]. Noncollinear magnetic ordering has the ability to harbor multimagnon excitations (bimagnon and trimagnon) [17,18,24]. The spectroscopic features of these multimagnon excitations have been investigated theoretically using resonant inelastic x-ray scattering (RIXS) at the K edge [24]. Additionally, multimagnon Raman spectra have been investigated for the model undistorted TLAF compound using torque equilibrium spin wave theory (TESWT) [14,17,18].

In frustrated magnetic systems such as TLAFs, competition between exchange interaction, anisotropic XXZ interaction, and Dzyaloshinskii-Moriya (DM) interaction enhance the spin fluctuation and cause the failure of linear spin wave theory. The linear spin wave theory approach gives

*These authors contributed equally to this work.

†Corresponding author: tdatta@augusta.edu

‡Corresponding author: yaodaox@mail.sysu.edu.cn

an incorrect ground state phase diagram. Furthermore, the $1/S$ corrected spin wave theory gives an unphysical ordering wave vector since the zero point energy cannot be properly accounted for [14,17]. To remedy these problems, Du *et al.* [14,16] established the TESWT, which considers the zero point energy and predicts a consistent result for the ground state phase diagram that agrees well with numerical calculations [25,26]. Furthermore, Ref. [17] extended the TESWT approach to include the DM interaction that was well fitted to the INS experimental data of the spin spiral TLAF Cs_2CuCl_4 [27]. The authors computed the interacting bimagnon and noninteracting trimagnon RIXS spectrum and found that both spatial anisotropy and DM interaction modify the RIXS spectrum at two inequivalent rotonlike points, $M(0, 2\pi/\sqrt{3})$ and $M'(\pi, \pi/\sqrt{3})$. Specifically, the existence of DM interaction stabilizes the spiral state and increases the energy of the roton minimum.

Due to the issues related to the experimental resolution, RIXS experimental studies on TLAFs are absent. Compared to RIXS, Raman experiments which probe multimagnon excitations in TLAFs are more prevalent [28,29]. Bimagnon excitations have been observed with Raman spectroscopy in the distorted TLAFs $\alpha\text{-SrCr}_2\text{O}_4$ [29] and $\alpha\text{-CaCr}_2\text{O}_4$ [28]. To study the magnon excitation spectrum in such spin spiral systems, Ref. [18] presented a TESWT analysis that considered the anisotropic XXZ interaction and the DM interaction to compute the polarized Raman spectra of Cs_2CuCl_4 and $\text{Ba}_3\text{CoSb}_2\text{O}_9$. It was reported that both the bimagnon and trimagnon excitations contribute to the Raman spectrum and are influenced by spatial anisotropy, XXZ interaction, and DM interaction [18]. In contrast to DM interaction, XXZ interaction plays a weaker role in stabilizing the helical state.

When the spiral order is 120° (or approximately around this value), the spin Casimir effect is negligible, and TESWT reverts back to spin wave theory. Since the spiral orders of $\alpha\text{-SrCr}_2\text{O}_4$ and $\alpha\text{-CaCr}_2\text{O}_4$ are close to 120° , we apply linear spin wave theory in this paper to analyze this class of TLAF compounds. Experimental data on the distorted TLAF compounds $\alpha\text{-SrCr}_2\text{O}_4$ and $\alpha\text{-CaCr}_2\text{O}_4$ suggest spiral ordering temperatures below 43 and 42.6 K, respectively [21,28–30]. For both $\alpha\text{-SrCr}_2\text{O}_4$ and $\alpha\text{-CaCr}_2\text{O}_4$, Raman scattering experiments have reported the presence of bimagnon excitation [28,29].

In this paper, we focus on the Raman spectrum of multimagnon excitations presented in the distorted TLAFs $\alpha\text{-SrCr}_2\text{O}_4$ [29] and $\alpha\text{-CaCr}_2\text{O}_4$ [28]. We perform a spin wave analysis of the ordered spiral state to compute the effects of the rotonlike M and M' points on the Raman spectrum of undistorted and distorted TLAFs. We study our model for a generic set of parameters to highlight the connection between the rotonlike points and their consequences for the bi- and trimagnon Raman excitation spectrum. Based on experimental data we propose a different set of magnetic interaction parameters to compute the Raman spectrum of $\alpha\text{-SrCr}_2\text{O}_4$ and use existing ones to predict the Raman spectrum of $\alpha\text{-CaCr}_2\text{O}_4$. We show that polarized Raman spectroscopy has the ability to distinguish the bimagnon excitation channel from the trimagnon response. This difference is evident from a couple of perspectives. From an energetic point of

view, the trimagnon signal always occurs at a higher energy than the bimagnon response. From a purely experimental scattering geometry setup, we find that the HH signal is more sensitive to the trimagnon excitation, whereas the HV signal has a more pronounced bimagnon response. Our theory suggests that the Raman scattering experiment captures both the bimagnon and trimagnon excitations according to the spin dynamic features revealed by the INS experiment [31].

This paper is organized as follows. In Sec. II, we introduce the Heisenberg model of the distorted TLAFs. In Sec. III, we compute the spin wave spectrum. In Sec. IV, we use spin wave theory to compute and discuss the physical implications of the bimagnon and trimagnon Raman spectra for our model Hamiltonian and for the real materials $\alpha\text{-LCr}_2\text{O}_4$ ($L=\text{Sr, Ca}$; using experimental data). In Sec. V, we provide our conclusions. In Appendixes A and B we list the equations for the classical ground state energy analysis and the polarized Raman scattering operator matrix elements, respectively.

II. MODEL

The spatially isotropic TLAF $\text{Ba}_3\text{CoSb}_2\text{O}_9$ exhibits a 120° spin spiral order which is well described by a spin-1/2 XXZ model [18,32–36]. For the anisotropic TLAFs, the ground states of Cs_2CuCl_4 and Cs_2CuBr_4 are long-range incommensurate spin spiral order in zero magnetic field [15,27,37]. The phases supported by these materials can be modeled using an antiferromagnet Heisenberg model with DM interaction [17,18,38]. The distorted TLAFs $\alpha\text{-SrCr}_2\text{O}_4$ and $\alpha\text{-CaCr}_2\text{O}_4$ are reported to have approximately 120° spin-3/2 spiral orders, with ordering wave vectors of $(\pi, \sim 4/3 \times 2\pi, 0)$ [20,30,31]. In spite of the spiral ordering in these compounds, DM interaction is absent.

The lattice structure of the distorted triangular lattice antiferromagnets $\alpha\text{-SrCr}_2\text{O}_4$ and $\alpha\text{-CaCr}_2\text{O}_4$ are shown in Fig. 1(a), which is an orthorhombic crystal structure belonging to the $Pm\bar{m}n$ space group (No. 59). The lattice distortion parameter is $d = 0.25$ (0.57) for $\alpha\text{-SrCr}_2\text{O}_4$ ($\alpha\text{-CaCr}_2\text{O}_4$), as shown in Table I. Such distortion results in a variety of exchange constants compared to a perfect TLAF, resulting in novel spin dynamic features in the presence of distorted TLAFs. Each unit cell of $\alpha\text{-SrCr}_2\text{O}_4$ and $\alpha\text{-CaCr}_2\text{O}_4$ contains four atoms with two inequivalent magnetic ions Cr^{3+} . The distortion creates shifts on the sites, generating four different nearest-exchange constants. Former studies have shown that the Hamiltonian of distorted TLAFs contains nearest-neighbor (NN) and next-nearest-neighbor (NNN) interactions [20,21,31].

We consider a model which can be easily mapped to the undistorted triangular lattice by setting $d = 0$. The Hamiltonian consists of the following interaction terms:

$$H = H_{\text{NN}} + H_{\text{NNN}} + H_{\text{int}} + H_{\text{an}}, \quad (1)$$

where H_{NN} , H_{NNN} , H_{int} , and H_{an} represent the nearest-neighbor exchange interaction, the next-nearest-neighbor exchange interaction, the interlayer exchange interaction, and

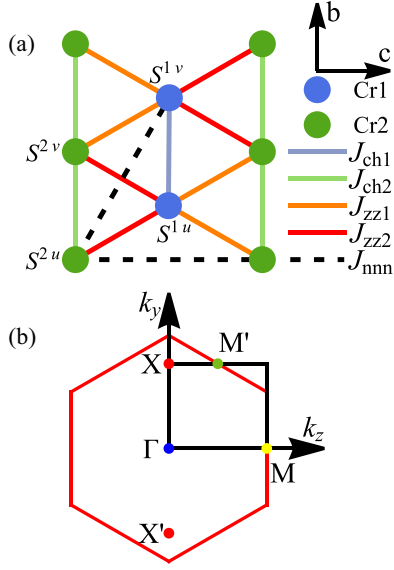


FIG. 1. (a) Unit cell of α -SrCr₂O₄ [31] and α -CaCr₂O₄ [20]. The positions of the four Cr³⁺ ions are (0,0,0), (0,0.5,0), (0, 0.25, 0.5 - 0.01d), and (0, 0.75, 0.5 + 0.01d), with site indices denoted by $i \in \{2u, 2v, 1u, 1v\}$, where d is the lattice distortion parameter. The two inequivalent Cr³⁺ ions are shown as blue Cr1 and green Cr2 dots. The spins are labeled as S^{1u} , S^{1v} , S^{2u} , and S^{2v} . (b) The black box is the first Brillouin zone (BZ) of the unit cell with four spins. The red hexagon is the first BZ of the undistorted TLAF, which contains only one spin in the unit cell. The high-symmetry points Γ , M , M' , X , and X' are shown in the BZ. The wave vectors are denoted by k_y and k_z .

the single-ion anisotropy. The detailed expressions for these interacting terms are given by

$$\begin{aligned}
 H_{\text{NN}} = & \sum_{\alpha,\beta} J_{ch1} \mathbf{S}_{\alpha\beta}^{1u} \cdot (\mathbf{S}_{\alpha\beta}^{1v} + \mathbf{S}_{(\alpha-1)\beta}^{1v}) \\
 & + J_{ch2} \mathbf{S}_{\alpha\beta}^{2u} \cdot (\mathbf{S}_{\alpha\beta}^{2v} + \mathbf{S}_{(\alpha-1)\beta}^{2v}) \\
 & + J_{zz1} \mathbf{S}_{\alpha\beta}^{1u} \cdot (\mathbf{S}_{\alpha(\beta-1)}^{2u} + \mathbf{S}_{\alpha(\beta-1)}^{2v}) \\
 & + J_{zz1} \mathbf{S}_{\alpha\beta}^{1v} \cdot (\mathbf{S}_{(\alpha+1)\beta}^{2u} + \mathbf{S}_{\alpha\beta}^{2v}) \\
 & + J_{zz2} \mathbf{S}_{\alpha\beta}^{1u} \cdot (\mathbf{S}_{\alpha\beta}^{2u} + \mathbf{S}_{\alpha\beta}^{2v}) \\
 & + J_{zz2} \mathbf{S}_{\alpha\beta}^{1v} \cdot (\mathbf{S}_{(\alpha+1)(\beta-1)}^{2u} + \mathbf{S}_{\alpha(\beta-1)}^{2v}), \quad (2)
 \end{aligned}$$

TABLE I. The parameter set choices for different distortion values utilized to compute the Raman spectra. \mathcal{P}_4 and \mathcal{P}_5 are the experimental (expt) parameter sets for the distorted TLAFs α -LCr₂O₄ (L =Sr, Ca) [21,31]. The penultimate row reports the fit parameters generated from our model based on the experimental data of Ref. [29]. The ordering wave vector $\mathbf{Q} = (Q_a, Q_b, 0)$, with $Q_a = \pi$ and Q_b , varies based on different parameter sets. \mathcal{P}_1 , \mathcal{P}_2 , and \mathcal{P}_3 are the model parameter sets, representing the 120° helical state. Below the Néel ordering temperature $T_N = 43$ K, α -SrCr₂O₄ forms an incommensurate helical order [20,29,30,39]. For α -CaCr₂O₄ the helical state forms below 42.6 K [21].

Parameter set	J_{ch1}	J_{ch2}	J_{zz1}	J_{zz2}	J_{NNN}	J_{int}	A	d	$Q_b/2\pi$
\mathcal{P}_1 (model)	1.0	1.0	1.0	1.0	0.01	0.01	0.01	0	4/3
\mathcal{P}_2 (model)	1.0	1.0	0.9	1.1	0.01	0.01	0.01	0.1	4/3
\mathcal{P}_3 (model)	1.0	1.0	0.8	1.2	0.01	0.01	0.01	0.2	4/3
\mathcal{P}_4 (expt, α -SrCr ₂ O ₄) [31]	5.2	4.9	3.8	6.0	0.35	0.02	0.01	0.25	1.3217
\mathcal{P}_5 (expt, α -CaCr ₂ O ₄) [21]	9.1	8.6	5.8	11.8	0.57	0.027	0	0.57	1.3317
\mathcal{P}_6 (proposed fit, α -SrCr ₂ O ₄)	6.5	7.5	4.6	7.9	0.45	0.02	0.06	0.25	1.3217
Valentine <i>et al.</i> (expt, α -SrCr ₂ O ₄) [29]	7.15	4.22	3.02	5.70				0.25	1.322

$$\begin{aligned}
 H_{\text{NNN}} = & \sum_{\alpha,\beta} J_{\text{NNN}} [\mathbf{S}_{\alpha\beta}^{2u} \cdot (\mathbf{S}_{\alpha(\beta+1)}^{2u} + \mathbf{S}_{\alpha\beta}^{1v} \\
 & + \mathbf{S}_{\alpha(\beta+1)}^{1v} + \mathbf{S}_{(\alpha-1)(\beta+1)}^{1u} + \mathbf{S}_{(\alpha-1)\beta}^{1u}) \\
 & + \mathbf{S}_{\alpha\beta}^{2v} \cdot (\mathbf{S}_{\alpha(\beta+1)}^{2v} + \mathbf{S}_{(\alpha+1)\beta}^{1u}) \\
 & + \mathbf{S}_{(\alpha+1)(\beta+1)}^{1u} + \mathbf{S}_{(\alpha-1)\beta}^{1v} + \mathbf{S}_{(\alpha-1)(\beta+1)}^{1v}) \\
 & + \mathbf{S}_{\alpha\beta}^{1u} \cdot \mathbf{S}_{\alpha(\beta+1)}^{1u} + \mathbf{S}_{\alpha\beta}^{1v} \cdot \mathbf{S}_{\alpha(\beta+1)}^{1v}], \quad (3)
 \end{aligned}$$

$$H_{\text{int}} = J_{\text{int}} \sum_{i,j} \mathbf{S}_{\alpha\beta} \cdot \mathbf{S}_{\alpha\beta+a}, \quad (4)$$

$$H_{\text{an}} = A \sum_{\alpha\beta} (S_{\alpha\beta}^b)^2. \quad (5)$$

The four different spin labels S^{2u} , S^{2v} , S^{1u} , and S^{1v} represent the four different sublattices in the unit cell of the distorted TLAFs. The parameters J_{ch1} , J_{ch2} , J_{zz1} , and J_{zz2} , corresponding to the exchange constants for NN interaction, are in the (b, c) plane. The three other parameters, J_{NNN} , J_{int} , and D , are for the NNN interaction, interlayer exchange interaction, and easy plane anisotropy, respectively. α and β in $\mathbf{S}_{\alpha\beta}$ are sites of the unit cell along the b direction and the c direction, respectively. See Table I for parameter values.

III. SPIN WAVE SPECTRUM

Inelastic neutron scattering experiments have been performed on α -LCr₂O₄ (L =Sr, Ca) to study their spin wave dynamics [21,31]. Neutron scattering studies provide us with the exchange constants and anisotropy parameters of these materials [21,31]. We compute the magnon dispersion for the spin-spiral ground state in the distorted TLAFs, which exhibits the ordering wave vector \mathbf{Q} rotating in the (a, c) plane and generating a helical spin order in its ground state configuration. The Hamiltonian in the local rotating basis is given by

$$\begin{aligned}
 H = & \sum_{i,j} J_{ij} [S_i^y S_j^y + \cos(\mathbf{Q} \cdot \mathbf{R}_{ij}) (S_i^x S_j^x + S_i^z S_j^z) \\
 & + \sin(\mathbf{Q} \cdot \mathbf{R}_{ij}) (S_i^z S_j^y - S_i^y S_j^z)] + A \sum_i (S_i^y)^2, \quad (6)
 \end{aligned}$$

where $\mathbf{R}_{ij} = \mathbf{R}_i - \mathbf{R}_j$ and J_{ij} is the exchange interaction between sites i and j . The first summation term contains the nearest-neighbor, the next-nearest-neighbor, and the interlayer exchange interactions, while the second summation contains the single-ion anisotropy. The spin components in the laboratory frame (a, b, c) were transformed into the rotating local frame basis (x, y, z) using the transformation [8]

$$\mathbf{S}_i = \begin{pmatrix} \cos(\mathbf{Q} \cdot \mathbf{R}_i) & 0 & \sin(\mathbf{Q} \cdot \mathbf{R}_i) \\ 0 & 1 & 0 \\ -\sin(\mathbf{Q} \cdot \mathbf{R}_i) & 0 & \cos(\mathbf{Q} \cdot \mathbf{R}_i) \end{pmatrix} \begin{pmatrix} S_i^x \\ S_i^y \\ S_i^z \end{pmatrix}. \quad (7)$$

Next, we perform the Holstein-Primakoff transformation to recast the spin label $S_i^{x,y,z}$ to the quasiparticle label given by

$$S_i^z = S - a_i^\dagger a_i, \quad S_i^- = a_i^\dagger \sqrt{2S - a_i^\dagger a_i}, \quad S_i^+ = (S_i^-)^\dagger, \quad (8)$$

where a_i^\dagger (a_i) is the magnon creation (annihilation) operator for a given site i . The quadratic spin wave Hamiltonian H_2 can then be expressed as

$$\begin{aligned} H_2 = & \sum_{i,j} J_{ij} S \left[\frac{1}{2} (-a_i a_j + a_i^\dagger a_j^\dagger + \text{H.c.}) \right. \\ & + \frac{1}{2} \cos(\mathbf{Q} \cdot \mathbf{R}_{ij}) (a_i a_j + a_i^\dagger a_j^\dagger + \text{H.c.}) \\ & \left. - \cos(\mathbf{Q} \cdot \mathbf{R}_{ij}) (a_i^\dagger a_i + a_j^\dagger a_j) \right] \\ & + \frac{AS}{2} \sum_i (-a_i a_i + a_i^\dagger a_i^\dagger + \text{H.c.}). \quad (9) \end{aligned}$$

After Fourier transformation the two interaction terms in H_2 are given by

$$\begin{aligned} H_2 = & \sum_{\mathbf{k}} \left\{ \sum_{i,j} J_{ij} S \left[\frac{1}{2} (-e^{i\mathbf{k} \cdot \mathbf{R}_{ij}} a_{\mathbf{k}_i} a_{-\mathbf{k}_j} + e^{i\mathbf{k} \cdot \mathbf{R}_{ij}} a_{\mathbf{k}_i}^\dagger a_{\mathbf{k}_j}^\dagger + \text{H.c.}) \right. \right. \\ & + \frac{1}{2} \cos(\mathbf{Q} \cdot \mathbf{R}_{ij}) (e^{i\mathbf{k} \cdot \mathbf{R}_{ij}} a_{\mathbf{k}_i} a_{-\mathbf{k}_j} + e^{i\mathbf{k} \cdot \mathbf{R}_{ij}} a_{\mathbf{k}_i}^\dagger a_{\mathbf{k}_j}^\dagger + \text{H.c.}) \\ & \left. - \cos(\mathbf{Q} \cdot \mathbf{R}_{ij}) (a_{\mathbf{k}_i}^\dagger a_{\mathbf{k}_i} + a_{\mathbf{k}_j}^\dagger a_{\mathbf{k}_j}) \right] \\ & \left. + \frac{AS}{2} \sum_i (-a_{\mathbf{k}_i} a_{-\mathbf{k}_i} + a_{\mathbf{k}_i}^\dagger a_{\mathbf{k}_i}^\dagger + \text{H.c.}) \right\}. \quad (10) \end{aligned}$$

Utilizing the numerical Bogoliubov transformation [40]

$$\begin{pmatrix} a_{\mathbf{k}_i} \\ a_{-\mathbf{k}_i}^\dagger \end{pmatrix} = \begin{pmatrix} u_{\mathbf{k}ip} & v_{\mathbf{k}ip} \\ v_{\mathbf{k}ip} & u_{\mathbf{k}ip} \end{pmatrix} \begin{pmatrix} b_{\mathbf{k}p} \\ b_{-\mathbf{k}p}^\dagger \end{pmatrix} = T_{\mathbf{k}} \begin{pmatrix} b_{\mathbf{k}p} \\ b_{-\mathbf{k}p}^\dagger \end{pmatrix}, \quad (11)$$

we diagonalize the Hamiltonian (10) to obtain the spin wave dispersion

$$T_{\mathbf{k}}^\dagger H_2 T_{\mathbf{k}} = \text{diag}(\omega_{\mathbf{k}_i}, -\omega_{\mathbf{k}_i}), \quad (12)$$

where diag represents the diagonal matrix of energy eigenvalues. As the ground states of α - LCr_2O_4 ($L=\text{Sr, Ca}$) are both close to a 120° order, we study three sets of model parameters ($\mathcal{P}_1, \mathcal{P}_2$, and \mathcal{P}_3) with different distortions d and ordering wave vectors \mathbf{Q} (see Table I for parameter choices). Assuming that exchange interaction is inversely proportional

to the bond length, we model the anisotropic interaction as J_{zz2} (J_{zz1}) $\approx J_{ch1}(1 \pm d)$ according to the parameters of α - LCr_2O_4 ($L=\text{Sr, Ca}$).

The single-magnon density of states (DOS) for $\mathcal{P}_1, \mathcal{P}_4$, and \mathcal{P}_5 in Table I are calculated. In Figs. 2(a)–2(c) we show the spin wave spectra for parameters sets \mathcal{P}_1 for the undistorted TLAf, \mathcal{P}_4 for α - SrCr_2O_4 , and \mathcal{P}_5 for α - CaCr_2O_4 . Inspecting the plots we can conclude that the local minimum points in the magnon dispersion are shifted by the presence of lattice distortion. It is reported that the local minima of the undistorted TLAf appear at the M and M' points, which are described as rotonlike points in literatures [41–43]. However, in the presence of distortion, the local minima points are shifted [see the black dots in Figs. 2(d)–2(f)]. Raman detection of rotonlike modes was performed by Wulferding *et al.* [28] for α - CaCr_2O_4 . The Raman spectrum shows a maximum around twice the roton energy. This is because the rotonlike points contribute to Van Hove singularities, causing a maxima in the DOS for one magnon. Since the bimagnon Raman signal comes from bimagnon excitation, which creates two magnons with inverse momentum, the maxima in Raman spectrum should reflect twice the energy of rotonlike points. However, the trimagnon Raman signal is from three-magnon excitation with zero total momentum, $\mathbf{k}_1 + \mathbf{k}_2 + \mathbf{k}_3 = 0$. The choice of wave vector for the trimagnon is not unique. Thus, the trimagnon Raman spectrum should be even broader.

The rotonlike points do not necessarily occur in the lowest energy branch. In Figs. 2(a) and 2(d), the M point of the undistorted TLAf shows the roton minimum in the second energy band. In contrast, the roton minimum for the M' point always occurs in the lowest energy band. In Fig. 2(d), the M' point shifts to the black points in the first Brillouin zone (BZ) of the distorted TLAf model due to the periodic condition. Each rotonlike point splits into four rotonlike points, as shown in Fig. 2(e) with enhanced distortion. Figure 2(f) indicates that the rotonlike points for the distorted TLAfs tend to spread when distortion d is increased. Finally, note that we have not considered magnon interactions. The Heisenberg model was treated at the quadratic linear spin wave level since the system is a spin-3/2 material. Thus, we expect quantum fluctuations to be suppressed. Additionally, the presence of multiple sublattices in the unit cell increases the algebraic complexity to pursue a fully interacting magnon calculation without contributing any additional understanding of the underlying spin dynamics behavior of the distorted TLAfs.

IV. RAMAN SPECTRUM

In this section we investigate the Raman spectra of TLAfs. We construct the Raman scattering operator for the bimagnon and trimagnon excitations. The bimagnon and trimagnon Raman intensity is related to the exchange scattering mechanism, which can be even stronger than the first-order spectrum [44]. First, we perform calculations of the polarized Raman spectra of α - SrCr_2O_4 and α - CaCr_2O_4 . Second, we give the physical implications of the bimagnon Raman signal and the rotonlike points in the single-magnon spin wave dispersion. We also discuss the trimagnon response. Finally, we fit the experimental data of α - SrCr_2O_4 with our unpolarized Raman spectrum and compute the unpolarized Raman spectrum of α - CaCr_2O_4 .

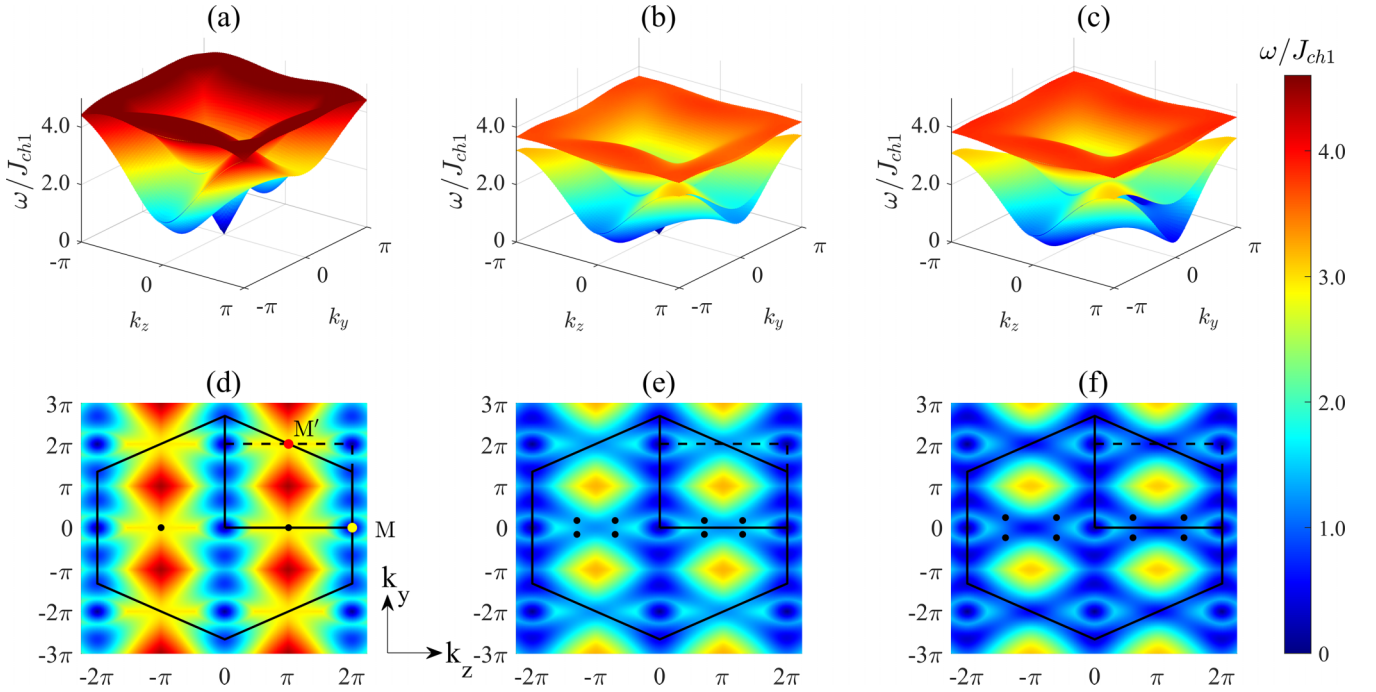


FIG. 2. Spin wave dispersion of the triangular lattice antiferromagnet. (a)–(c) Spin wave dispersions for parameter sets \mathcal{P}_1 , \mathcal{P}_4 , and \mathcal{P}_5 , respectively. There are four branches of energy for each parameter set as the unit cell contains four sublattices. (d)–(f) One of the four energy branches with the lowest energy which correspond to (a)–(c). $M(0, 0, 2\pi)$ and $M'(0, \pi, 2\pi)$ are the rotonlike points of the undistorted triangular antiferromagnet for \mathcal{P}_1 . The roton minimum energy can be observed in rotonlike points indicated by the black dots. We observe the roton energy minimum at different spin wave dispersion branches for various parameter sets (see Table I). Distortion results in M' becoming the only rotonlike point which splits into four different points in the spin wave dispersion. Enhanced distortion spreads the split rotonlike points [indicated by the eight black dots in (e)] into four different directions in momentum space [see (f)].

A. Raman scattering operator

Raman intensity is highly sensitive to the polarization direction of the incident and outgoing light in crystals [45–50]. The Raman scattering operator for TLAFs contains weight coefficients which vary based on the polarization direction. The dependence on polarization can be expressed as a matrix [18]. The two TLAF compounds α - SrCr_2O_4 and α - CaCr_2O_4 belong to the P_{mmn} (D_{2h}) space group. The interlayer exchange interaction is very weak compared to the intralayer coupling strength (see Table I). Thus, we consider the magnetic Cr^{3+} ions within the (b, c) plane to be described by C_{2v} symmetry. The Raman active modes of the C_{2v} point group are $A_1 + A_2$. These modes are described by the same Raman tensor as the $A_g + B_{1g}$ Raman active modes of D_{2h} symmetry. Following the procedure of Ref. [46], we derive the polarization coefficient matrix $P_{ij}(\theta, \phi)$, which is given by [18]

$$P_{ij}(\theta, \phi) = \epsilon_{\text{in}}(\theta) \begin{pmatrix} p_2 & 0 & 0 \\ 0 & p_1 & 0 \\ 0 & 0 & p_3 \end{pmatrix} \epsilon_{\text{out}}^T(\phi) \eta_{ij}^{A_1} + \epsilon_{\text{in}}(\theta) \begin{pmatrix} 0 & 0 & 0 \\ 0 & 0 & p_4 \\ 0 & p_4 & 0 \end{pmatrix} \epsilon_{\text{out}}^T(\phi) \eta_{ij}^{A_2}. \quad (13)$$

In Fig. 3(a) we show the scattering geometry that is used to perform the calculation. The incident and outgoing light vectors are expressed as $\epsilon_{\text{in}}(\theta) = (0, \cos(\theta), \sin(\theta))$ and $\epsilon_{\text{out}}(\phi) = (0, \cos(\phi), \sin(\phi))$.

The total polarized Raman scattering operator \hat{O} is given by

$$\begin{aligned} \hat{O}(\theta, \phi) &= \sum_{i,j} P_{ij}(\theta, \phi) J_{ij} \mathbf{S}_i \cdot \mathbf{S}_j \\ &= \hat{O}_2(\theta, \phi) + \hat{O}_3(\theta, \phi). \end{aligned} \quad (14)$$

In the above expression, the polarized bimagnon and trimagnon Raman scattering operators \hat{O}_2 and \hat{O}_3 , respectively, include only the nearest-neighbor and next-nearest-neighbor interactions. The expressions for \hat{O}_2 and \hat{O}_3 are given by

$$\begin{aligned} \hat{O}_2(\theta, \phi) &= \sum_{i,j} J'_{ij} P_{ij}(\theta, \phi) S \left[\frac{1}{2} (-a_i a_j + a_i^\dagger a_j^\dagger + \text{H.c.}) \right. \\ &\quad \left. + \frac{1}{2} \cos(\mathbf{Q} \cdot \mathbf{R}_{ij}) (a_i a_j + a_i^\dagger a_j^\dagger + \text{H.c.}) \right. \\ &\quad \left. - \cos(\mathbf{Q} \cdot \mathbf{R}_{ij}) (a_i^\dagger a_i + a_j^\dagger a_j) \right], \end{aligned} \quad (15)$$

$$\begin{aligned} \hat{O}_3(\theta, \phi) &= \sum_{i,j} J'_{ij} P_{ij}(\theta, \phi) \sqrt{\frac{S}{2}} \sin(\mathbf{Q} \cdot \mathbf{R}_{ij}) \\ &\quad \times (a_i a_j^\dagger a_j + a_i^\dagger a_j^\dagger a_j - a_i^\dagger a_i a_j - a_i^\dagger a_i a_j^\dagger), \end{aligned} \quad (16)$$

where the in-plane interaction J'_{ij} includes J_{ch1} , J_{ch2} , J_{z1} , J_{z2} , and J_{NNN} . After Fourier transformation, we

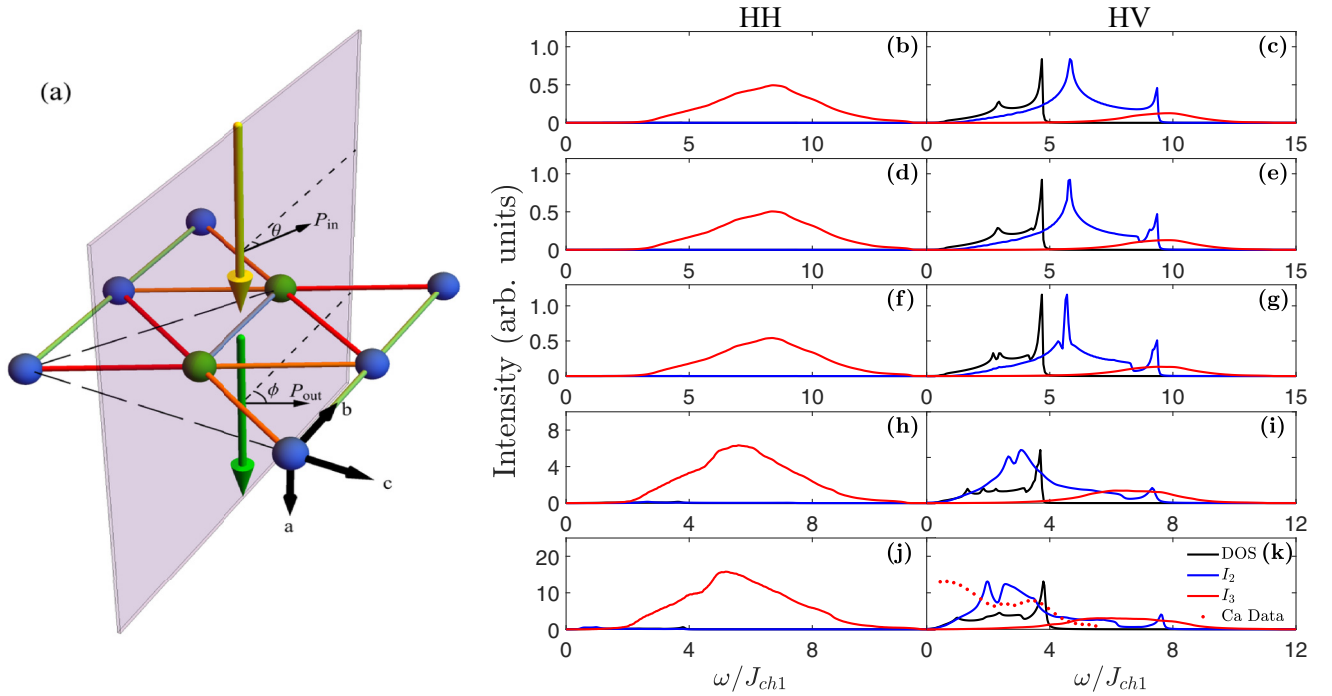


FIG. 3. (a) Raman scattering geometry. Incident light is always assumed to be along the a axis. The angles θ and ϕ are defined as displayed. (b)–(k) The polarized bimagnon $I_2(\omega, \theta, \phi)$ and trimagnon $I_3(\omega, \theta, \phi)$ Raman spectra. Each row refers to the parameter choice \mathcal{P}_i , with $i = 1, \dots, 5$, from top to bottom (see Table I). The first column represents HH polarization with $(\theta, \phi) = (0, 0)$. The second column is HV polarization with $(\theta, \phi) = (0, \frac{\pi}{2})$. All the calculated Raman intensities are computed by applying $p_1 = p_2 = p_3 = p_4 = 1$ and a small broadening parameter $0^+ = 0.02$ meV. The black solid line is the single-magnon density of states. Red dots are extracted using WEBPLOTDIGITIZER [51] from the Raman experiment in circular RL polarization reported for α - CaCr_2O_4 in Ref. [28].

obtain

$$\hat{O}_2(\theta, \phi) = \sum_{i,j \in u.c.} J'_{ij} P_{ij}(\theta, \phi) S \sum_{\mathbf{k}} \left[\frac{1}{2} (-e^{i\mathbf{k} \cdot \mathbf{R}_{ij}} a_{\mathbf{k}i} a_{-\mathbf{k}j} + e^{i\mathbf{k} \cdot \mathbf{R}_{ij}} a_{\mathbf{k}i} a_{\mathbf{k}j}^\dagger + \text{H.c.}) \right. \\ \left. + \frac{1}{2} \cos(\mathbf{Q} \cdot \mathbf{R}_{ij}) (e^{i\mathbf{k} \cdot \mathbf{R}_{ij}} a_{\mathbf{k}i} a_{-\mathbf{k}j} + e^{i\mathbf{k} \cdot \mathbf{R}_{ij}} a_{\mathbf{k}i} a_{\mathbf{k}j}^\dagger + \text{H.c.}) - \cos(\mathbf{Q} \cdot \mathbf{R}_{ij}) (a_{\mathbf{k}i}^\dagger a_{\mathbf{k}i} + a_{\mathbf{k}j}^\dagger a_{\mathbf{k}j}) \right] \quad (17)$$

and

$$\hat{O}_3(\theta, \phi) = \sum_{i,j \in u.c.} J'_{ij} P_{ij}(\theta, \phi) \sqrt{\frac{S}{2N}} \sin(\mathbf{Q} \cdot \mathbf{R}_{ij}) \left(\sum_{\mathbf{k}_2 + \mathbf{k}_3 = \mathbf{k}_1} e^{i\mathbf{k}_2 \cdot \mathbf{R}_{ij}} a_{\mathbf{k}_1j}^\dagger a_{\mathbf{k}_2i} a_{\mathbf{k}_3j} + \sum_{\mathbf{k}_1 + \mathbf{k}_2 = \mathbf{k}_3} e^{-i\mathbf{k}_2 \cdot \mathbf{R}_{ij}} a_{\mathbf{k}_1j}^\dagger a_{\mathbf{k}_2i}^\dagger a_{\mathbf{k}_3j} \right. \\ \left. - \sum_{\mathbf{k}_2 + \mathbf{k}_3 = \mathbf{k}_1} e^{-i\mathbf{k}_2 \cdot \mathbf{R}_{ij}} a_{\mathbf{k}_1i}^\dagger a_{\mathbf{k}_2j} a_{\mathbf{k}_3i} - \sum_{\mathbf{k}_1 + \mathbf{k}_2 = \mathbf{k}_3} e^{i\mathbf{k}_2 \cdot \mathbf{R}_{ij}} a_{\mathbf{k}_1i}^\dagger a_{\mathbf{k}_2j}^\dagger a_{\mathbf{k}_3i} \right). \quad (18)$$

Next, we apply the Bogoliubov transformation to derive the final expression for the polarized bimagnon and trimagnon Raman scattering operators. They are given by

$$\hat{O}_2(\theta, \phi) = \sum_{\mathbf{k}} \sum_{p,q} M_{\mathbf{k}}^{pq} (b_{\mathbf{k}p} b_{-\mathbf{k}q} + b_{-\mathbf{k}p}^\dagger b_{\mathbf{k}q}^\dagger), \quad (19)$$

$$\hat{O}_3(\theta, \phi) = \sum_{\mathbf{k}, \mathbf{l}} \sum_{p,q,t} N_{\mathbf{k}\mathbf{l}}^{pqt} (b_{\mathbf{k}p} b_{-\mathbf{k}-\mathbf{l}q} b_{\mathbf{l}t} + b_{-\mathbf{k}p}^\dagger b_{\mathbf{k}+1q}^\dagger b_{-\mathbf{l}t}^\dagger), \quad (20)$$

where the expressions for the Raman matrix elements $M_{\mathbf{k}}^{pq}$ and $N_{\mathbf{k}\mathbf{l}}^{pqt}$ are supplied in Appendix B. Note that in the polarized trimagnon Raman scattering operator $\hat{O}_3(\theta, \phi)$, the momentum symbol transforms as $\mathbf{k}_1 \rightarrow \mathbf{k}$, $\mathbf{k}_2 \rightarrow -\mathbf{k} - \mathbf{l}$, and $\mathbf{k}_3 \rightarrow \mathbf{l}$, where \mathbf{k} and \mathbf{l} belong to the first BZ.

B. Polarized Raman spectrum

We can use the polarized bimagnon and trimagnon Raman scattering operators introduced in the previous section to construct the bimagnon Green's function $G_2(\omega, \theta, \phi)$ and the trimagnon Green's function $G_3(\omega, \theta, \phi)$. The corresponding definitions are given by

$$G_2(\omega, \theta, \phi) = -i \int_{-\infty}^{+\infty} dt e^{i\omega t} \langle T \hat{O}_2^\dagger(t, \theta, \phi) \hat{O}_2(0, \theta, \phi) \rangle, \quad (21)$$

$$G_3(\omega, \theta, \phi) = -i \int_{-\infty}^{+\infty} dt e^{i\omega t} \langle T \hat{O}_3^\dagger(t, \theta, \phi) \hat{O}_3(0, \theta, \phi) \rangle. \quad (22)$$

Thus, the polarized bimagnon Raman intensity $I_2(\omega, \theta, \phi)$ and trimagnon Raman intensity $I_3(\omega, \theta, \phi)$ can be written as

$$I_2(\omega, \theta, \phi) = -\frac{1}{\pi} \text{Im} G_2(\omega, \theta, \phi) = -\frac{1}{\pi} \text{Im} \left[2 \sum_{\mathbf{k}, p, q} \frac{|M_{\mathbf{k}}^{pq}|^2}{\omega - \omega_{\mathbf{k}p} - \omega_{-\mathbf{k}q} + i0^+} \right] \quad (23)$$

and

$$I_3(\omega, \theta, \phi) = -\frac{1}{\pi} \text{Im} G_3(\omega, \theta, \phi) = -\frac{1}{\pi} \text{Im} \left[6 \sum_{\mathbf{k}, \mathbf{l}} \sum_{p, q, t} \frac{|N_{\mathbf{k}\mathbf{l}}^{pqt}|^2}{\omega - \omega_{\mathbf{k}p} - \omega_{-\mathbf{k}-\mathbf{l}q} - \omega_{\mathbf{l}t} + i0^+} \right]. \quad (24)$$

The polarized Raman intensities depend on the polarization direction of the incident and outgoing lights. In the subsequent calculations, we will fix the incident light polarization angle θ to be equal to zero, and the outgoing light polarization angle ϕ will vary according to the polarization we choose [see Fig. 3(a)].

The polarized Raman spectrum of the distorted TLAF is shown in Fig. 3. The vertical axis shows the Raman intensity, and the horizontal axis shows the energy rescaled in units of ω/J_{ch1} . The Raman spectrum for α -SrCr₂O₄ was computed using the model described in Sec. II using the parameters stated in Table I. The magnetic exchange interactions in α -CaCr₂O₄ are different from those in its Sr counterpart. Whereas the Sr compound has only one J_{NNN} , the Ca compound has four. Hence, to keep the calculation tractable for α -CaCr₂O₄ we used an effective J_{NNN} which has only one next-nearest-neighbor exchange interaction as input. This effective value is obtained by taking the average of the four different next-nearest-neighbor exchange energies reported in Ref. [21].

In the first column on the right in Fig. 3 we show the results of the HH polarized channel. As expected, the bimagnon signals vanish since the Raman scattering operator \hat{O}_2 commutes with the Hamiltonian H_2 . Thus, only the trimagnon excitation contributes to the Raman intensity in the HH polarized case. For all the parameter sets that were studied, we observed a pronounced trimagnon continuum vanishing at triple the energy maximum of a single-magnon excitation. We find that as the spatial interaction anisotropy $J_{zz1}-J_{zz2}$ increases, the trimagnon continua in Fig. 3 undergo a spectral downshift for the HH polarization.

In the second column on the right in Fig. 3 we show the results of the HV polarization. These plots display the DOS, the bimagnon Raman intensity, and the trimagnon Raman intensity. In HV polarization, we observe both the bimagnon and trimagnon signals. The bimagnon intensity I_2 is relatively stronger than the trimagnon signal. It occupies an energy region from 0 to approximately 10 for parameter choices of

$\mathcal{P}_1, \mathcal{P}_2$, and \mathcal{P}_3 . As an example, we observe that the I_2 signal of the undistorted TLAF shows a peak at 5.82 and an additional peak at 9.36 in Fig. 3(c).

The DOS displays two peaks, a small low-energy peak and a strong high-energy peak. The DOS signal influences the bimagnon Raman spectrum. At the rotonlike point, the density of magnons is substantially enhanced compared to the other locations in the BZ since $\nabla_{\mathbf{k}}E = 0$. Since the velocity vanishes, we observe a strong signal in the DOS. From Fig. 3(c) we notice that this happens at 2.94, which is where the low-energy DOS peak is located. This generates the stronger low-energy bimagnon Raman intensity. Thus, this signal is a direct consequence of the rotonlike point in the TLAF system. For the undistorted lattice, the 5.82 bimagnon peak arises from both the rotonlike wave vector points, M and M' . I_2 shows a 9.36 peak due to the one-magnon maximum energy, which vanishes before 5.

In an undistorted TLAF rotonlike points (M and M') on the Raman spectrum are equivalent. However, as spatial anisotropy is increased (a fact that naturally occurs in real materials), the Raman spectrum becomes sensitive. Note that in Fig. 3(g), the anisotropy generates a nonzero DOS contribution at 2.70 from only the M' point. The M point, on the other hand, has zero contribution (confirmed by calculation). With increasing distortion, the spatial anisotropy changes the spin wave dispersion structure at the M point, thereby causing $\nabla_{\mathbf{k}}E \neq 0$. Thus, the M point ceases to behave as a rotonlike point. This is the physical origin of the bimagnon energy peak at 5.34 for \mathcal{P}_3 . Hence, we see that Raman spectroscopy has the ability to provide insight into the physical nature of the rotonlike point in the TLAF system.

In Figs. 3(g), 3(i), and 3(k) the bimagnon signal splits into two peaks when the lattice distortion is enhanced. All the parameter sets from \mathcal{P}_3 to \mathcal{P}_5 support this peak-splitting effect. The lower-energy peak of this two-peak signal originates from the M' rotonlike point. However, it is not obvious what the physical origin of the higher-energy peak within this two-peak signal is. Our calculations suggest that the first bimagnon peak

for parameter set \mathcal{P}_4 (\mathcal{P}_5) in Fig. 3(i) [Fig. 3(k)] appears at 1.33 (0.99), which is exactly twice the energy of the local minima shown in Fig. 2(e) [Fig. 2(f)].

In addition, to distinguish the different rotonlike points due to the presence of anisotropy, the Raman spectrum has a selective response based on the polarization channels, HH and HV. As noted earlier, the HH channel contribution is exclusively from the trimagnon signal. For the HV channel, the opposite holds true. While there is a weak trimagnon signal, the overwhelming strength comes from the bimagnon excitation. The nearest-neighbor and the next-nearest-neighbor interactions have the same weight along all directions in the trimagnon Raman scattering operator for the HH polarization. However, interactions along the b axis make no contribution to producing the trimagnon Raman signal for the HV polarization. Therefore, the trimagnon Raman signal intensity for the HV polarization is observed to be weaker than those for HH polarization. Similar to the HH channel, the HV channel also shows a spectral downshift for the trimagnon Raman spectrum with increasing distortion.

C. Unpolarized Raman spectrum

At present there is no consensus on the value of the material parameters that describe the magnetic properties of α -SrCr₂O₄ [14,29] (see the fifth and sixth rows in Table I). Motivated by the experimental data of Valentine *et al.* [29], we compute the unpolarized Raman spectrum of α -SrCr₂O₄. To calculate the unpolarized spectrum, we integrate the incident and outgoing light polarization angles θ and ϕ in the Green's function. The resulting expression is given by

$$G_\epsilon^u(\omega) = -i \int_{-\infty}^{+\infty} dt \int_0^\pi d\theta \int_0^\pi d\phi \times e^{i\omega t} \langle T \hat{O}_\epsilon^\dagger(t, \theta, \phi) \hat{O}_\epsilon(0, \theta, \phi) \rangle, \quad (25)$$

$$I_\epsilon^u(\omega) = -\frac{1}{\pi} \text{Im} G_\epsilon(\omega),$$

where $I_\epsilon(\omega)$ represents the unpolarized Raman spectrum with $\epsilon = 2$ and 3, referring to the bimagnon and the trimagnon Green's function channels. The results are presented in Fig. 4(a).

Upon fitting the experimental data of Valentine *et al.* [29], we obtain a different set of parameters, presented as \mathcal{P}_6 in Table I. This data set reproduces the spin wave dispersion (not shown here) of α -SrCr₂O₄, including capturing the high-energy magnon branches. It also adequately reproduces the experimental unpolarized Raman spectrum of α -SrCr₂O₄. Upon fitting, the spectrum displays two prominent peaks, one at 20 meV and the other at 40 meV. The 20 meV signal is primarily composed of the bimagnon channel. However, the 40 meV signal is predominantly trimagnon. Overall, the trimagnon intensity is stronger than the bimagnon intensity. This feature of the unpolarized spectrum can allow one to distinguish these two different multimagnon excitations. Competition between magnetic interaction parameters results in an approximately 120° spiral order in α -SrCr₂O₄ (see calculation details in Appendix A). Therefore, our calculation suggests that the 15 meV Raman shift signal originates from the bimagnon excitation. The signal on the 40 meV Raman

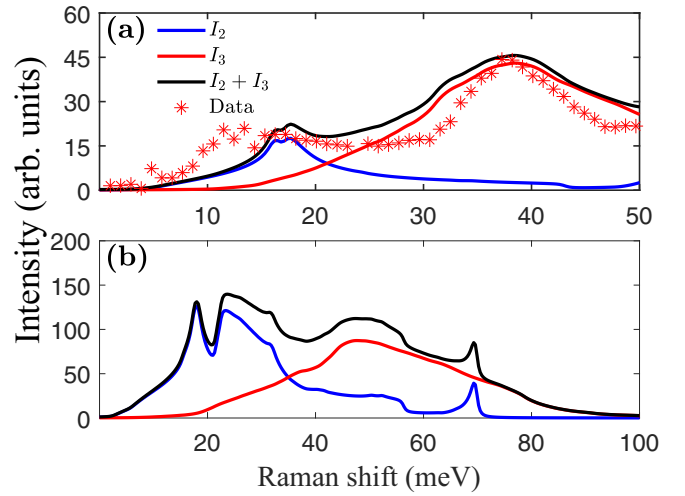


FIG. 4. Unpolarized Raman spectrum of (a) α -SrCr₂O₄ and (b) α -CaCr₂O₄. (a) The blue line is the bimagnon Raman spectrum I_2 . The red line corresponds to the trimagnon Raman spectrum I_3 . The black line is the total Raman spectrum $I_2 + I_3$. Both I_2 and I_3 are the results of our fitting procedure. We report a set of interaction parameters, \mathcal{P}_6 , generated from our model and based on the experimental data reported in Ref. [29] (displayed as red asterisks) in Table I. The calculation utilizes $p_1 = p_2 = p_3 = 1$ and $p_4 = 0.42$. (b) Predicted unpolarized Raman spectrum of α -CaCr₂O₄. The spectrum was calculated based on the experimental parameter set \mathcal{P}_5 reported in Ref. [21]. For α -CaCr₂O₄, I_2 and I_3 were computed with $p_1 = p_2 = p_3 = p_4 = 1$.

shift arises from the trimagnon excitation rather than the bimagnon excitation. In Fig. 4(b), we present our prediction for the unpolarized Raman spectrum of α -CaCr₂O₄. Compared to the Sr compound, the Ca compound exhibits a more significant peak-splitting effect on the bimagnon Raman signal.

V. CONCLUSIONS

Motivated by the Raman experimental data for TLAFs, we have investigated the consequences of the nontrivial rotonlike points on the bimagnon and trimagnon excitation spectra of α -SrCr₂O₄ and α -CaCr₂O₄. Utilizing Raman experimental data for α -SrCr₂O₄, we fit our model to propose a different set of magnetic interaction parameters. This set of parameters is able to consistently reproduce both the inelastic neutron scattering spectrum and the Raman spectrum of α -SrCr₂O₄. Based on our calculations, we demonstrated that Raman spectroscopy is sensitive to the behavior of the rotonlike M and M' points that have been proposed to exist in TLAF systems. Additionally, we found that the polarization sensitivity of the incoming beam in the Raman spectrum can allow one to distinguish the multimagnon excitation channels (bimagnon versus trimagnon). We observed that the trimagnon Raman signal is the higher-energy peak compared to the bimagnon signal. Furthermore, with increasing distortion the peak-splitting effect becomes more prominent in the bimagnon Raman signal.

According to our calculation, the 40 meV Raman signal in the experimental Raman scattering data originates from the trimagnon excitation. The bimagnon excitation could also

make some minor contribution to the 40 meV signal. It is worth noting that our proposed magnetic interaction parameters were obtained from fitting with the experimental data of the unpolarized Raman spectrum of α -SrCr₂O₄. Nevertheless, the proposed set of parameters still gives the approximate 120° spiral order. This is a further validation of our fitting procedure. We also predicted the unpolarized Raman spectrum of α -CaCr₂O₄. Compared to the Sr compound, α -CaCr₂O₄ has a more intense lattice distortion and stronger in-plane and interlayer exchange interactions. We hope that our theoretical investigation will motivate the TLAf community to further study the connection between multimagnon excitation and rotonlike points of the TLAfs.

ACKNOWLEDGMENTS

We thank N. Drichko for sharing the unpolarized Raman experimental data for α -SrCr₂O₄ and M. Songvilay for helpful discussions about magnetic interaction param-

eters for α -SrCr₂O₄. We acknowledge M. He and C. Shan for useful discussions. This project is supported by Grants No. NKRDPC-2022YFA1402802, No. NKRDPC-2018YFA0306001, No. NSFC-92165204, and No. NSFC-11974432; the Shenzhen International Quantum Academy (Grant No. SIQA202102); and Leading Talent Program of Guangdong Special Projects (Grant No. 201626003). T.D. acknowledges the funding support from Sun Yat-Sen University Grant No. OEMT-2019-KF-04 and the hospitality of KITP at the University of California, Santa Barbara. Part of this research was completed at KITP and was supported in part by the National Science Foundation under Grant No. NSF PHY-1748958.

APPENDIX A: CLASSICAL GROUND STATE ANALYSIS

The classical ground state energy of α -SrCr₂O₄ is given by

$$E_0(\mathbf{Q}) = NS^2 \sum_{i,j} J_{ij} \cos(\mathbf{Q} \cdot \mathbf{R}_{ij}). \quad (\text{A1})$$

The stabilized spiral order results in

$$\frac{\partial E_0}{\partial Q_b} = -NS^2 \left[J_{ch1} \sin\left(\frac{1}{2}Q_b\right) + J_{ch2} \sin\left(\frac{1}{2}Q_b\right) + J_{zz1} \sin\left(\frac{1}{4}Q_b\right) + J_{zz2} \sin\left(\frac{1}{4}Q_b\right) + 6J_{NNN} \sin\left(\frac{3}{4}Q_b\right) \right] = 0. \quad (\text{A2})$$

By applying the magnetic interaction parameters \mathcal{P}_6 in Table I, the solution to Eq. (A2) is $Q_b/2\pi = 1.3031$, which is close to the experimental value in Ref. [31]. We thus keep using $Q_b/2\pi = 1.3217$ for \mathcal{P}_6 .

APPENDIX B: POLARIZED RAMAN SCATTERING MATRIX ELEMENTS

The detailed expressions for $M_{\mathbf{k}}^{pq}$ and $N_{\mathbf{kl}}^{pqt}$ in Eqs. (19) and (20) are

$$M_{\mathbf{k}}^{pq} = \frac{1}{2} J_{ij} P_{ij}(\theta, \phi) S \left[-e^{i\mathbf{k} \cdot \mathbf{R}_{ij}} (u_{\mathbf{k} ip} - v_{\mathbf{k} ip})(u_{-\mathbf{k} jq} - v_{-\mathbf{k} jq}) + \cos(\mathbf{Q} \cdot \mathbf{R}_{ij}) e^{i\mathbf{k} \cdot \mathbf{R}_{ij}} (u_{\mathbf{k} ip} + v_{\mathbf{k} ip})(u_{-\mathbf{k} jq} + v_{-\mathbf{k} jq}) - \cos(\mathbf{Q} \cdot \mathbf{R}_{ij}) (u_{\mathbf{k} ip} v_{-\mathbf{k} iq} + v_{\mathbf{k} ip} u_{-\mathbf{k} iq} + u_{\mathbf{k} jp} v_{-\mathbf{k} jq} + v_{\mathbf{k} jp} u_{-\mathbf{k} jq}) \right], \quad (\text{B1})$$

$$N_{\mathbf{kl}}^{pqt} = \frac{1}{6} J_{ij} P_{ij}(\theta, \phi) \sin(\mathbf{Q} \cdot \mathbf{R}_{ij}) \sqrt{\frac{S}{2N}} \left[e^{i\mathbf{k} \cdot \mathbf{R}_{ij}} (u_{\mathbf{k} ip} + v_{\mathbf{k} ip})(u_{-\mathbf{k}-1 jq} v_{1 jt} + u_{1 jq} v_{-\mathbf{k}-1 jt}) - e^{-i\mathbf{k} \cdot \mathbf{R}_{ij}} (u_{\mathbf{k} jp} + v_{\mathbf{k} jp})(u_{-\mathbf{k}-1 iq} v_{1 it} + u_{1 iq} v_{-\mathbf{k}-1 it}) + e^{i(-\mathbf{k}-1) \cdot \mathbf{R}_{ij}} (u_{-\mathbf{k}-1 ip} + v_{-\mathbf{k}-1 ip})(u_{1 jq} v_{\mathbf{k} jt} + u_{\mathbf{k} jq} v_{1 jt}) - e^{-i(-\mathbf{k}-1) \cdot \mathbf{R}_{ij}} (u_{-\mathbf{k}-1 jp} + v_{-\mathbf{k}-1 jp})(u_{1 iq} v_{\mathbf{k} it} + u_{\mathbf{k} iq} v_{1 it}) + e^{i\mathbf{l} \cdot \mathbf{R}_{ij}} (u_{1 ip} + v_{1 ip})(u_{\mathbf{k} jq} v_{-\mathbf{k}-1 jt} + u_{-\mathbf{k}-1 jq} v_{\mathbf{k} jt}) - e^{-i\mathbf{l} \cdot \mathbf{R}_{ij}} (u_{1 jp} + v_{1 jp})(u_{\mathbf{k} iq} v_{-\mathbf{k}-1 it} + u_{-\mathbf{k}-1 iq} v_{\mathbf{k} it}) \right]. \quad (\text{B2})$$

- [1] H. Kadowaki, K. Ubukoshi, K. Hirakawa, J. L. Martínez, and G. Shirane, Experimental study of new type phase transition in triangular lattice antiferromagnet VCl₂, *J. Phys. Soc. Jpn.* **56**, 4027 (1987).
- [2] M. Poirier, F. Damay, C. Martin, J. Robert, and S. Petit, Spin dynamics in the geometrically frustrated multiferroic CuCrO₂, *Phys. Rev. B* **81**, 104411 (2010).
- [3] R. Ishii, S. Tanaka, K. Onuma, Y. Nambu, M. Tokunaga, T. Sakakibara, N. Kawashima, Y. Maeno, C. Broholm, D. P. Gautreaux, J. Y. Chan, and S. Nakatsuji, Successive phase

transitions and phase diagrams for the quasi-two-dimensional easy-axis triangular antiferromagnet Rb₄Mn(MoO₄)₃, *Europhys. Lett.* **94**, 17001 (2011).

- [4] Y. Shirata, H. Tanaka, A. Matsuo, and K. Kindo, Experimental Realization of a Spin-1/2 Triangular-Lattice Heisenberg Antiferromagnet, *Phys. Rev. Lett.* **108**, 057205 (2012).
- [5] T. Jolicœur and J. C. Le Guillou, Spin-wave results for the triangular Heisenberg antiferromagnet, *Phys. Rev. B* **40**, 2727 (1989).

- [6] R. R. P. Singh and D. A. Huse, Three-Sublattice Order in Triangular- and Kagomé-Lattice Spin-Half Antiferromagnets, *Phys. Rev. Lett.* **68**, 1766 (1992).
- [7] B. Bernu, P. Lecheminant, C. Lhuillier, and L. Pierre, Exact spectra, spin susceptibilities, and order parameter of the quantum Heisenberg antiferromagnet on the triangular lattice, *Phys. Rev. B* **50**, 10048 (1994).
- [8] A. L. Chernyshev and M. E. Zhitomirsky, Spin waves in a triangular lattice antiferromagnet: Decays, spectrum renormalization, and singularities, *Phys. Rev. B* **79**, 144416 (2009).
- [9] M. Swanson, J. T. Haraldsen, and R. S. Fishman, Critical anisotropies of a geometrically frustrated triangular-lattice antiferromagnet, *Phys. Rev. B* **79**, 184413 (2009).
- [10] R. S. Fishman and S. Okamoto, Noncollinear magnetic phases of a triangular-lattice antiferromagnet and of doped CuFeO_2 , *Phys. Rev. B* **81**, 020402(R) (2010).
- [11] O. A. Starykh, W. Jin, and A. V. Chubukov, Phases of a Triangular-Lattice Antiferromagnet Near Saturation, *Phys. Rev. Lett.* **113**, 087204 (2014).
- [12] P. H. Y. Li, R. F. Bishop, and C. E. Campbell, Quasiclassical magnetic order and its loss in a spin- $\frac{1}{2}$ Heisenberg antiferromagnet on a triangular lattice with competing bonds, *Phys. Rev. B* **91**, 014426 (2015).
- [13] E. A. Ghioldi, A. Mezio, L. O. Manuel, R. R. P. Singh, J. Oitmaa, and A. E. Trumper, Magnons and excitation continuum in XXZ triangular antiferromagnetic model: Application to $\text{Ba}_3\text{CoSb}_2\text{O}_9$, *Phys. Rev. B* **91**, 134423 (2015).
- [14] Z. Z. Du, H. M. Liu, Y. L. Xie, Q. H. Wang, and J.-M. Liu, Spin Casimir effect in noncollinear quantum antiferromagnets: Torque equilibrium spin wave approach, *Phys. Rev. B* **92**, 214409 (2015).
- [15] E. Ghorbani, L. F. Tocchio, and F. Becca, Variational wave functions for the $s = \frac{1}{2}$ Heisenberg model on the anisotropic triangular lattice: Spin liquids and spiral orders, *Phys. Rev. B* **93**, 085111 (2016).
- [16] Z. Z. Du, H. M. Liu, Y. L. Xie, Q. H. Wang, and J.-M. Liu, Magnetic excitations in quasi-one-dimensional helimagnets: Magnon decays and influence of interchain interactions, *Phys. Rev. B* **94**, 134416 (2016).
- [17] S. Jin, C. Luo, T. Datta, and D.-X. Yao, Torque equilibrium spin wave theory study of anisotropy and Dzyaloshinskii-Moriya interaction effects on the indirect k -edge RIXS spectrum of a triangular lattice antiferromagnet, *Phys. Rev. B* **100**, 054410 (2019).
- [18] C. Shan, S. Jin, T. Datta, and D.-X. Yao, Torque equilibrium spin wave theory of raman scattering in an anisotropic triangular lattice antiferromagnet with Dzyaloshinskii-Moriya interaction, *Phys. Rev. B* **103**, 024417 (2021).
- [19] O. A. Starykh, Unusual ordered phases of highly frustrated magnets: A review, *Rep. Prog. Phys.* **78**, 052502 (2015).
- [20] S. Toth, B. Lake, S. A. J. Kimber, O. Pieper, M. Reehuis, A. T. M. N. Islam, O. Zaharko, C. Ritter, A. H. Hill, H. Ryll, K. Kiefer, D. N. Argyriou, and A. J. Williams, 120° helical magnetic order in the distorted triangular antiferromagnet α - CaCr_2O_4 , *Phys. Rev. B* **84**, 054452 (2011).
- [21] S. Toth, B. Lake, K. Hradil, T. Guidi, K. C. Rule, M. B. Stone, and A. T. M. N. Islam, Magnetic Soft Modes in the Distorted Triangular Antiferromagnet α - CaCr_2O_4 , *Phys. Rev. Lett.* **109**, 127203 (2012).
- [22] M. Mourigal, W. T. Fuhrman, A. L. Chernyshev, and M. E. Zhitomirsky, Dynamical structure factor of the triangular-lattice antiferromagnet, *Phys. Rev. B* **88**, 094407 (2013).
- [23] U. Falk, A. Furrer, H. U. Güdel, and J. K. Kjems, Inelastic neutron scattering study of magnetic interactions in $\text{CsMn}_x\text{Mg}_{1-x}\text{Br}_3$. I. Spin waves in CsMnBr_3 , *Phys. Rev. B* **35**, 4888 (1987).
- [24] C. Luo, T. Datta, Z. Huang, and D.-X. Yao, Signatures of indirect k -edge resonant inelastic x-ray scattering on magnetic excitations in a triangular-lattice antiferromagnet, *Phys. Rev. B* **92**, 035109 (2015).
- [25] Zheng Weihong, R. H. McKenzie, and R. R. P. Singh, Phase diagram for a class of spin- $\frac{1}{2}$ Heisenberg models interpolating between the square-lattice, the triangular-lattice, and the linear-chain limits, *Phys. Rev. B* **59**, 14367 (1999).
- [26] P. Hauke, T. Roscilde, V. Murg, J. I. Cirac, and R. Schmied, Modified spin-wave theory with ordering vector optimization: Spatially anisotropic triangular lattice and $J_1J_2J_3$ model with Heisenberg interactions, *New J. Phys.* **13**, 075017 (2011).
- [27] R. Coldea, D. A. Tennant, and Z. Tylczynski, Extended scattering continua characteristic of spin fractionalization in the two-dimensional frustrated quantum magnet Cs_2CuCl_4 observed by neutron scattering, *Phys. Rev. B* **68**, 134424 (2003).
- [28] D. Wulferding, K.-Y. Choi, P. Lemmens, A. N. Ponomaryov, J. van Tol, A. T. M. N. Islam, S. Toth, and B. Lake, Softened magnetic excitations in the $s = 3/2$ distorted triangular antiferromagnet α - CaCr_2O_4 , *J. Phys.: Condens. Matter* **24**, 435604 (2012).
- [29] M. E. Valentine, S. Koohpayeh, M. Mourigal, T. M. McQueen, C. Broholm, N. Drichko, S. E. Dutton, R. J. Cava, T. Birol, H. Das, and C. J. Fennie, Raman study of magnetic excitations and magnetoelastic coupling in α - SrCr_2O_4 , *Phys. Rev. B* **91**, 144411 (2015).
- [30] S. E. Dutton, E. Climent-Pascual, P. W. Stephens, J. P. Hodges, A. Huq, C. L. Broholm, and R. J. Cava, Helical magnetism and structural anomalies in triangular lattice α - SrCr_2O_4 , *J. Phys.: Condens. Matter* **23**, 246005 (2011).
- [31] M. Songvilay, S. Petit, E. Suard, C. Martin, and F. Damay, Spin dynamics in the distorted triangular lattice antiferromagnet α - SrCr_2O_4 , *Phys. Rev. B* **96**, 024416 (2017).
- [32] T. Susuki, N. Kurita, T. Tanaka, H. Nojiri, A. Matsuo, K. Kindo, and H. Tanaka, Magnetization Process and Collective Excitations in the $S = 1/2$ Triangular-Lattice Heisenberg Antiferromagnet $\text{Ba}_3\text{CoSb}_2\text{O}_9$, *Phys. Rev. Lett.* **110**, 267201 (2013).
- [33] D. Yamamoto, G. Marmorini, and I. Danshita, Quantum Phase Diagram of the Triangular-Lattice XXZ Model in a Magnetic Field, *Phys. Rev. Lett.* **112**, 127203 (2014).
- [34] D. Yamamoto, G. Marmorini, and I. Danshita, Erratum: Quantum Phase Diagram of the Triangular-Lattice XXZ Model in a Magnetic Field [*Phys. Rev. Lett.* **112**, 127203 (2014)], *Phys. Rev. Lett.* **112**, 259901(E) (2014).
- [35] G. Koutroulakis, T. Zhou, Y. Kamiya, J. D. Thompson, H. D. Zhou, C. D. Batista, and S. E. Brown, Quantum phase diagram of the $S = \frac{1}{2}$ triangular-lattice antiferromagnet $\text{Ba}_3\text{CoSb}_2\text{O}_9$, *Phys. Rev. B* **91**, 024410 (2015).
- [36] D. Yamamoto, G. Marmorini, and I. Danshita, Microscopic Model Calculations for the Magnetization Process of Layered Triangular-Lattice Quantum Antiferromagnets, *Phys. Rev. Lett.* **114**, 027201 (2015).

- [37] T. Ono, H. Tanaka, H. Aruga Katori, F. Ishikawa, H. Mitamura, and T. Goto, Magnetization plateau in the frustrated quantum spin system Cs_2CuBr_4 , *Phys. Rev. B* **67**, 104431 (2003).
- [38] J. O. Fjærestad, W. Zheng, R. R. P. Singh, R. H. McKenzie, and R. Coldea, Excitation spectra and ground state properties of the layered spin- $\frac{1}{2}$ frustrated antiferromagnets Cs_2CuCl_4 and Cs_2CuBr_4 , *Phys. Rev. B* **75**, 174447 (2007).
- [39] L. C. Chapon, P. Manuel, F. Damay, P. Toledano, V. Hardy, and C. Martin, Helical magnetic state in the distorted triangular lattice of $\alpha\text{-CaCr}_2\text{O}_4$, *Phys. Rev. B* **83**, 024409 (2011).
- [40] J. Van Hemmen, A note on the diagonalization of quadratic boson and fermion Hamiltonians, *Z. Phys. B* **38**, 271 (1980).
- [41] O. A. Starykh, A. V. Chubukov, and A. G. Abanov, Flat spin-wave dispersion in a triangular antiferromagnet, *Phys. Rev. B* **74**, 180403(R) (2006).
- [42] W. Zheng, J. O. Fjærestad, R. R. P. Singh, R. H. McKenzie, and R. Coldea, Excitation spectra of the spin- $\frac{1}{2}$ triangular-lattice Heisenberg antiferromagnet, *Phys. Rev. B* **74**, 224420 (2006).
- [43] W. Zheng, J. O. Fjærestad, R. R. P. Singh, R. H. McKenzie, and R. Coldea, Anomalous Excitation Spectra of Frustrated Quantum Antiferromagnets, *Phys. Rev. Lett.* **96**, 057201 (2006).
- [44] P. A. Fleury, S. P. S. Porto, and R. Loudon, Two-Magnon Light Scattering in Antiferromagnetic MnF_2 , *Phys. Rev. Lett.* **18**, 658 (1967).
- [45] T. Moriya, Theory of light scattering by magnetic crystals, *J. Phys. Soc. Jpn.* **23**, 490 (1967).
- [46] K. Sugawara and I. Yamada, Raman scattering study of the triangular-lattice antiferromagnet VCl_2 , *J. Phys.: Condens. Matter* **5**, 1427 (1993).
- [47] M. Suzuki, I. Yamada, H. Kadowaki, and F. Takei, A Raman scattering investigation of the magnetic ordering in the two-dimensional triangular lattice antiferromagnet LiCrO_2 , *J. Phys.: Condens. Matter* **5**, 4225 (1993).
- [48] F. Vernay, T. P. Devereaux, and M. J. P. Gingras, Raman scattering for triangular lattices spin-1/2 Heisenberg antiferromagnets, *J. Phys.: Condens. Matter* **19**, 145243 (2007).
- [49] N. Perkins and W. Brenig, Raman scattering in a Heisenberg $S = \frac{1}{2}$ antiferromagnet on the triangular lattice, *Phys. Rev. B* **77**, 174412 (2008).
- [50] N. B. Perkins, G.-W. Chern, and W. Brenig, Raman scattering in a Heisenberg $S = \frac{1}{2}$ antiferromagnet on the anisotropic triangular lattice, *Phys. Rev. B* **87**, 174423 (2013).
- [51] A. Rohatgi, WEBPLOTDIGITIZER, version 4.6, <https://automeris.io/WebPlotDigitizer/> (2022).